ELSEVIER

Contents lists available at ScienceDirect

Acta Astronautica

journal homepage: www.elsevier.com/locate/actaastro



Research paper

Computed tomographic imaging spectroscopy for the measurement of re-entry break-up and demise

Byrenn Birch

Institute for Advanced Engineering and Space Sciences, University of Southern Queensland, West Street, Toowoomba, 4350, Queensland, Australia



ARTICLE INFO

Keywords:
Re-entry
Demise
Break-up
Imaging spectroscopy
Computed tomographic imaging spectroscopy

ABSTRACT

Spectral measurements of re-entry events are essential to the development and validation of the numerical models of re-entry that are required for safe and sustainable space industries. Imaging spectrometers are the dominant instrument for re-entry capsule measurements; and, while they have had some success in re-entry demise observations, they cannot discriminate between multiple objects with overlapping spectral signatures. These successes have required substantial separation of the objects along the dispersion-normal axis. To overcome this restrictive requirement, spectral imaging methods that are suitable for measurements of objects with overlapping spectral signatures are required. In this work, the viability of the computed tomographic imaging spectroscopy (CTIS) technique for re-entry applications is demonstrated. A prototype CTIS instrument was developed and used to measure scenes replicating aspects of the spatial and spectral properties of re-entry break-up fields; a spatiospectral field significantly different to those previously investigated using CTIS. A new CTIS calibration method which is suitable for in-situ fieldwork calibration was developed. The prototype instrument was able to reconstruct both the high-frequency spatial features and the narrowband spectral features of the test scene, demonstrating its potential for material identification during re-entry. Through measurements of a known-radiance source, CTIS was shown to be capable of resolving spectral irradiance in wavelength and amplitude, should the spectral sensitivity of the instrument be suitable. These newly validated capabilities of CTIS could enable its application in broader contexts, such as the high-enthalpy flows produced in shock tunnels and plasma facilities. Practical recommendations to develop the prototype into an observation-ready instrument design are provided.

1. Introduction

Remote scientific measurements of re-entry events, including demise, are dominated by spectral measurements. The spectral instruments used in these observations can be broadly categorised into three categories: (1) non-imaging spectrometers; (2) imaging spectrometers; and (3) filtered imaging. Non-imaging spectrometers are typically used for their high spectral resolution, however as the entire scene is focused on a fibre, all spatial resolution is lost. Imaging spectrometers can be used to obtain both spatial and spectral information, however the spectral resolution is typically lower than that of non-imaging spectrometers (see [1,2] for instrumentation specification charts). Filtered imagery can be used to obtain spatial information for a scene, however these instruments lack the ability to discern between multiple spectral emissions within the same bandpass.

Imaging spectrometers are the dominant instrument type for reentry capsule measurements; and, while have had some success in re-entry demise observations, they cannot discriminate between multiple objects with overlapping spectral signatures. Typically, imaging spectrometers are designed to disperse a spectrum perpendicular to the target's velocity vector. When two or more objects are on the same dispersion axis their spectral images will overlap, therefore, it is not possible to discriminate between their spectral signatures. For example, consider the re-entry of the Hayabusa capsule and spacecraft bus is presented in Fig. 1 [1]. Spectral imaging of this scene would disperse the spectra vertically, which would prohibit the analysis of objects within the debris field due to wavelength confusion. This was the case in [3], where there were also cases of wavelength confusion (signal interference) between the Hayabusa capsule and the demising spacecraft bus. The scientific objective of the Hayabusa re-entry was to measure the spectral signatures of the capsule, which, due to spatial separation of the capsule and the bus debris field, was successful. Despite the present inability to resolve individual objects within the debris field, spectral measurements of re-entry demise have been key to understanding when events occur in time [4].

E-mail address: byrenn.birch@unisq.edu.au.

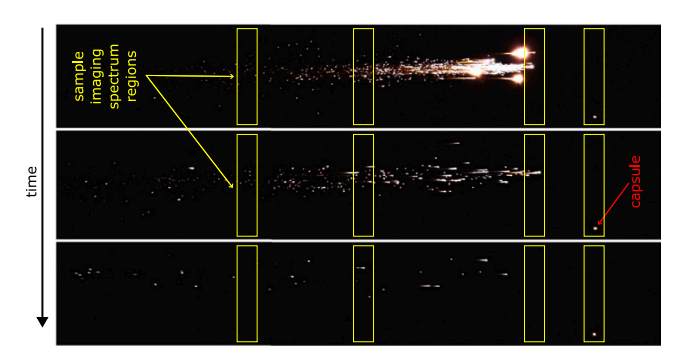


Fig. 1. Still frames of the Hayabusa re-entry showing the capsule and the demising bus debris field. Yellow rectangles are used to indicate fields of view discrete spectrums for an imaging spectrometer with a dispersion axis along the long edge of the rectangles. (For interpretation of the references to colour in this figure legend, the reader is referred to the web version of this article.) *Source:* Adapted from [1].

Through use of fibre-reformatting imaging spectroscopy (FRIS), it is possible to obtain a spatially resolved spectrum without object confusion. This is achieved by using a fibre bundle to collect light from a scene and reformat the light into a line for imaging on a sensor. The NASA SCIFLI 4DIS imager [5] is an example of an FRIS instrument where hex-packed (0.955 mm across flats) circular fibres are used to collect light from a scene and reformatted to a 12.96 mm wide line for imaging on a sensor. By mapping each fibre, the image scene can be reconstructed from spectral measurements. While the 4DIS imager has excellent spatial resolution (500 µrad per fibre), the fibre fill factor is 51%, therefore half of a scene's spatial content is not recorded. Of significance for demise measurements, the physical size of the hexpacked bundle limits the field of view of the 4DIS instrument to 0.458°. Additionally, while the 4DIS spectral resolution is high, a reconstructed image of the scene is limited to 216 pixels - approximately the resolution of a 15×15 image. Therefore, in the re-entry context, FRIS is best suited to spatially resolved measurements of single objects rather than being applied to multibody fields such as those seen in re-entry demise.

Multispectral imaging is possible, however these are typically an extended colour filter array construction limited to a small number of spectral bands with each bandpass too wide for quality re-entry demise measurements. Hyperspectral imaging is widely used in remote sensing applications to simultaneously obtain spatial and spectral information from a scene, data which is combined into a hypercube. Four approaches are used to construct the hypercube: (1) spatial scanning; (2) spectral scanning; (3) snapshot; and (4) spatiospectral scanning. In spatial, spectral and spatiospectral scanning, the hypercube is constructed from data that is not simultaneously acquired, therefore is not suitable for dynamic scenes such as re-entry demise. Snapshot hyperspectral imaging has a number of variants, including FRIS and computed tomographic imaging spectroscopy (CTIS). Snapshot imagers are typically more complex than scanning imagers and should be designed for a specific application to fully realise the snapshot light throughput advantage [6]. When coupled with a suitable sensor, snapshot methods are usually faster than scanning systems, therefore are of great interest to applications where acquisition speed is a key requirement [7]. The ability of snapshot imagers to obtain spatiospectral information in a single exposure provides the possibility of movie-mode operation to capture rare or unique events [8]. The large data volumes collected by snapshot systems often limits onboard hypercube construction, however the data can be readily processed offline. This data volume is not a concern for re-entry demise as there are no requirements for real- or near-time processing. This paper presents the design and analysis of a CTIS instrument to overcome the aforementioned limitations of existing spectral imaging systems, thereby enabling the spatially and spectrally resolved measurement of re-entry demise.

2. Spectral and spatial properties of a re-entry break-up field

To design an instrument for re-entry demise measurements, it is necessary to understand the spatiospectral properties of a re-entry break-up field. Spatially, the field is sparsely populated with bright objects (see Fig. 1), therefore an instrument must be capable of resolving a field with high-frequency spatial features. Most point sources shown in Fig. 1 are saturated, which enabled the wake for each object to be imaged. Saturation is not permitted in the CTIS spectral data, thus this figure presents information unlikely to be present in a CTIS image. It is likely that the CTIS instrument will resolve only the high-intensity point sources, not the low-intensity wakes. Spectrally, each object can contain: (1) broadband Planck-like radiance from the object's hot surfaces; (2) narrowband radiance from shock heated gases, ablation products, melting, and other demise processes; and (3) signal attenuation effects from the atmosphere. Sample irradiance spectra from the ATV-1 [9] and Hayabusa2 [10] re-entries are shown in Fig. 2.

For ATV-1 (Fig. 2(a)), the spectrum is from a non-imaging spectrometer for times around the main explosive break-up event. Therefore, the data lacks spatial information. This spectrum shows significant narrowband features from metals, which is typical of a demise event. Oxides of aluminium and titanium are also common, as are sodium, magnesium, lithium and potassium [11–13]; the latter two often indicative of a battery ablation. While the specific bandpass of interest will be observation dependent, many spacecraft materials have spectral emissions in the near-UV and visible wavelengths.

While the spectral irradiance presented in Figs. 2(a) and 2(b) are for different wavelength regions, the spectrum for an object deliberately designed to survive re-entry, such as the Hayabusa2 sample return capsule, is more simple than that of a demising object as it lacks the emission from metals and oxides. Instead, the Hayabusa2 spectrum (Fig. 2(b)) demonstrates a stronger Planck-like radiance from the capsule's thermal protection system, with some narrowband features from shock-heated gases. Fig. 2(b) also demonstrates the affect of atmospheric attenuation on the measured spectral irradiance.

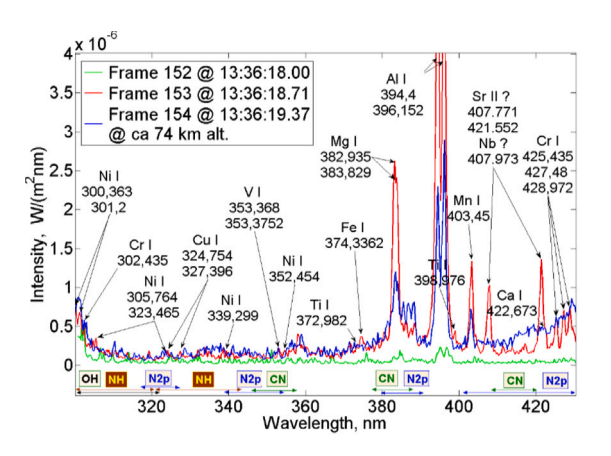
Like the spatial image of Fig. 1, the spectral content of a reentry break-up field contains high-frequency features. To resolve the narrowband emission features, spectral resolutions of the order of a few nanometres or less are used for re-entry observations [1,2]. Therefore, a hyperspectral imager for re-entry demise measurements must be capable of resolving a field with high-frequency spatial features and narrowband spectral features with a comparable spectral resolution. As CTIS uses a diffractive element, target bandpasses at shorter wavelengths can facilitate a CTIS designs with higher spectral resolution than for longer wavelength bandpasses.

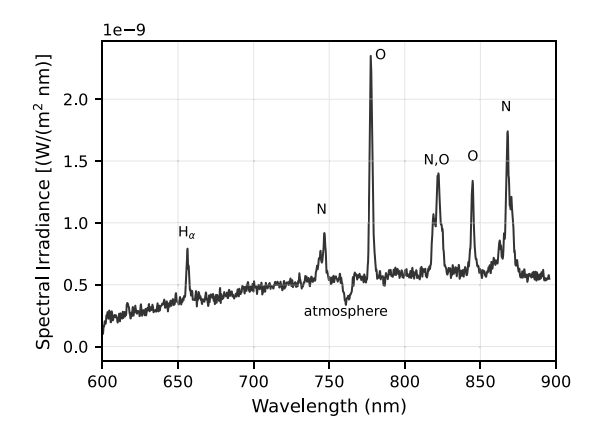
3. Computed tomographic imaging spectroscopy

3.1. Background

The computed tomographic imaging spectroscopy (CTIS) technique is a snapshot hyperspectral imaging technique that records the spatial and spectral information of a scene on a single focal plane array. This is achieved by a limited angle projection of the scene's spatiospectral information, which is then reconstructed via tomographic methods to obtain an interpretable $\{x, y, \lambda\}$ hypercube. The major advantages of this system are the snapshot acquisition of the spatiospectral information and that the system can be made compact [14], which is important for space-limited applications such as airborne re-entry observations. Because the CTIS method uses a projection approach on a single sensor, the spatial and spectral resolutions are coupled, therefore a trade-off between the two is required — an increase in spatial resolution results in a decrease in spectral resolution and vice versa.

The basic optical layout of the CTIS instrument is shown in Fig. 3. A field lens forms an image of the scene at the field stop, which is a 2-D aperture that is used to limit the size of the zeroth-order image





(a) ATV-1 re-entry spectral irradiance at around the main explosion event [9].

(b) Hayabusa2 sample return capsule. Adapted from [10].

Fig. 2. Samples spectral irradiance from destructive (ATV-1) [9] and non-destructive (Hayabusa2) [10] re-entries. *Source:* Adapted from [9,10].

on the sensor. The light which passes through the field stop is then collimated and then passed through a 2-D diffractive optical element (DOE). The diffracted images are then re-imaged onto the sensor by the re-imaging lens, with these diffracted images forming a limited view set of the scene's spatiospectral information (see Fig. 5).

Use of the CTIS technique has been investigated for a diverse range of applications, including: medical and biological imaging [15,16]; agriculture [17–19]; generic natural scenes [20]; and astronomy [8]. Further studies that focus on improving the tomographic reconstruction algorithms typically utilise synthetic data which is acquired from scanning hyperspectral cameras [7]; numerically generated data [6]; scenes formed by a RGB screen [21]; or the use of a laboratory test scene [22]. The scenes investigated in these studies lack the high-frequency narrowband spectral features that are present in re-entry demise events. Studies of scenes comprised of multiple high-intensity point sources were not identified. Should the CTIS technique be capable of reconstructing scenes with high-frequency spectral features, it could be applied to high-enthalpy ground-based testing such as in shock tunnels and plasma facilities.

3.2. Prototype instrument design

The generalised optical layout of a CTIS instrument is shown in Fig. 3 where light is collected by the field lens and focused at a field stop to limit the size of the zeroth-order image on the focal plane array (FPA). Light which passes through the field stop propagates to a collimating lens, then the dispersing optic and a re-imaging lens. In the present work: the objective is a $f=25\,\mathrm{mm}$ f/1.4 lens (Edmund 67715); the field stop is a 6 mm square; the collimating lens is $f=100\,\mathrm{mm}$ f/2.8 lens (Edmund 86410) and re-imaging lens is a Sony $f=50\,\mathrm{mm}$ f/1.8 lens; the dispersion element a 2D DOE; and the sensor a Sony α 7s III. Dispersion modes $m=\{-1,0,1\}$ are imaged in a 3 × 3 configuration (see Fig. 5). This arrangement results in a 13.7° × 13.7° square field of view with the wavelength range limited to the visible spectrum by the sensor. The spatial field of view was chosen to maximise the spatial field of view achievable with the DOE used, thereby achieving a FOV that is of realistic size for a re-entry demise measurement.

The spatial field of view of the CTIS instrument (θ) is determined by the field stop size (L_{FS}) and the focal length of the field lens as

$$\theta = 2 \tan^{-1} \left(\frac{L_{FS}}{2 f_1} \right) \tag{1}$$

The physical size of the zeroth-order sub-image is determined by the field stop size and the magnification (M) of the system per

$$\hat{L}_{FS} = L_{FS} \times |M| = L_{FS} \times \left| -\frac{f_3}{f_2} \right| \tag{2}$$

Considering an on-axis point source and a rectangular diffraction pattern, the vector displacement of each non-zero diffracted order from its zeroth-order spot on the sensor is described by

$$\vec{\Delta r}_{\text{sensor}} = \begin{pmatrix} \Delta x \\ \Delta y \end{pmatrix} = f_3 \begin{pmatrix} \tan \left| \sin^{-1} \left(\frac{m_x \lambda}{d_x} \right) \right| \\ \tan \left| \sin^{-1} \left(\frac{m_y \lambda}{d_y} \right) \right| \end{pmatrix}$$
(3)

where Δx and Δy are the displacements in the x and y directions on the sensor; m_x and m_y are the diffraction orders in the x and y directions; and d_x and d_y are the DOE grating periods in the x and y directions. Since there can be no overlap of the CTIS sub-images, the minimum wavelength (λ_{\min}) for the system is

$$\lambda_{\min} = \max \left\{ \frac{d_x}{m_x} \sin \left[\tan^{-1} \left(\frac{L_{FS,x}}{f_2} \right) \right] \\ \frac{d_y}{m_y} \sin \left[\tan^{-1} \left(\frac{L_{FS,y}}{f_2} \right) \right] \right\}$$
 (4)

While it is possible to design a DOE with zero first order intensity, off design wavelengths will have some first-order intensity. Therefore, Eq. (4) can be simplified using m=1 since the first-order diffracted images are the closest to the zeroth-order image, with the equation ensuring that the first-order diffracted images are outside the zeroth-order image on the sensor. Per traditional spectral imaging, it is also important to ensure that higher-order modes do not overlap with other modes. Further, the physical size of the sensor (L_s) limits the maximum wavelength (λ_{\max}) that can be imaged by

$$\lambda_{\max} = \min \left(\frac{\frac{d_{x}}{m_{x}} \sin \left[\tan^{-1} \left(\frac{1}{2} \left\{ \frac{L_{S,x}}{f_{3}} - \frac{L_{FS,x}}{f_{2}} \right\} \right) \right]}{\frac{d_{y}}{m_{y}} \sin \left[\tan^{-1} \left(\frac{1}{2} \left\{ \frac{L_{S,y}}{f_{3}} - \frac{L_{FS,y}}{f_{2}} \right\} \right) \right]} \right)$$
 (5)

The design dispersion in $nmmm^{-1}$ can be found by differentiating Eq. (3) and later transformed to $nmpixel^{-1}$ by dividing by the number of pixels per millimetre on the sensor. The differential of Eq. (3) is nonlinear, however for many practical design bandpasses the differential can be approximated as linear. For the prototype instrument, the analytically determined design dispersion is $1.6255 \, nm \, pixel^{-1}$ at $450 \, nm$ and $1.6031 \, nm \, pixel^{-1}$ at $650 \, nm$. These values are within 1% of the experimentally determined dispersion of $1.618 \, nm \, pixel^{-1}$; a value which was assumed constant in this work.

The vector displacement presented in Eq. (3) is for rays incident normal to the DOE, which is the case for an on-axis point source. Off axis sources within the field of view will have an angle of incidence on the DOE, which will affect the vector displacement of the diffracted orders on the sensor and therefore may appear on a different wavelength slice in the hypercube. The maximum error in the displacement occurs

Fig. 3. Schematic of the CTIS instrument showing rays from a point source at infinity in the centre of the field of view.

for point sources at the edge of the field of view, thus the maximum shift of the focused spot relative to an on-axis point source is calculated using

$$\Delta = \pm f_3 \left(\tan \left[\sin^{-1} \left(\frac{m \lambda}{d} + \sin \left[\frac{\theta}{2} \frac{f_1}{f_2} \right] \right) \right] - \tan \left[\sin^{-1} \left(\frac{m \lambda}{d} \right) \right] - \frac{\theta}{2} \frac{f_1}{f_2} \right)$$
(6)

Evaluating Eq. (6) for the prototype instrument results in $\Delta = \pm 12.3 \, \mu m$ at $\lambda = 550 \, nm$. This result is of the order of the effective pixel size (16.8 μm) and therefore off-axis aliasing effects are not significant for the prototype instrument. Chromatic aberrations will also contribute to aliasing, however these effects have not been quantified.

As a prototype instrument, there are two major design limitations which should be overcome for a future instrument: (1) the DOE; and (2) the sensor. The DOE used in this work is a Holoeye DE804 which is designed to disperse an incident beam at 650 nm into a 5×5 dot matrix pattern of equal intensities. As only the inner 3×3 dots are used for imaging, 16 of the 25 dots are not used, which is approximately 64% of the available light at the design wavelength being diffracted to unused orders. Another significant limitation of the DOE used is its physical size of $4.6\,\mathrm{mm}$ square, which limits the efficiency of the instrument. These two DOE limitations can be overcome by using a DOE with a larger physical size that produces a more efficient dot matrix pattern for the CTIS instrument.

The DOE separation angle between each dot of the matrix is 7.5° at 650 nm, which is equivalent to a 204 lines mm⁻¹ grating. The distance between a pixel in the zeroth-order image and a pixel in the firstorder image is presented in Fig. 4 for selected re-imaging lens focal lengths and a 6 mm square field stop. Fig. 4(a) shows that without field stop magnification, the regions on the sensor for the zeroth and first order images overlap for all visible wavelengths at $f = 30 \,\mathrm{mm}$, with significant overlap also present for $f = 50 \,\mathrm{mm}$. At $f = 75 \,\mathrm{mm}$, the distance between the zeroth and first-order images increases such that the first-order diffraction is off-sensor for wavelengths longer than 585 nm. Through 0.5× magnification of the field stop (Fig. 4(b)), the distance between the zeroth and first-order images is sufficient to separate the first-order diffraction from the zeroth-order image, while also retaining the first-order images on the sensor. Due to lens availability, a 50 mm focal length re-imaging lens and a 100 mm collimating lens were selected for the prototype. In addition to a physically larger DOE with only the required orders, increasing the DOE diffraction angle would be advantageous. For example, a direct swap to a 300 line/mm equivalent DOE would nearly fill the short axis of the sensor and increase the spectral resolution by a factor of 1.5. Custom DOE designs should also consider reducing the efficiency of the (0,0) order to reduce the zerothorder image size on the sensor, however this will negatively impact the efficiency of the $(\pm 1,0)$ and $(0,\pm 1)$ orders.

As shown in Fig. 4, the diffraction distances are large therefore a large sensor is required. The Sony α 7s III was selected and has a sensor size of 35.6 \times 23.8 mm with a raw image resolution of 4256 \times 2848 pixels, resulting in a design dispersion of approximately 0.8 nm pixel⁻¹. However, the sensor is not monochromatic and has utilises a RGGB colour filter array which reduces the effective spectral resolution to

approximately $1.6\,\mathrm{nm\,pixel}^{-1}$ for each colour channel. Note that this is the design resolution. The actual resolution is dependent on the SNR of the image at the degree of multiplexing in present in the image [6]. Each colour channel was extracted from the raw image to create three separate images with a resolution of 2128×1424 pixels. Future designs of the CTIS instrument should use a monochromatic sensor to increase the spectral resolution and sensitivity of the instrument. The Sony α 7s III operates a rolling shutter. The sensor for a CTIS instrument in a re-entry demise application should be a global shutter so that the entire scene is captured at the same time. The analysis presented herein considers the green pixels of the sensor.

3.3. Structure of the CTIS image

The image formed on the image sensor by the prototype instrument consists of nine sub-images, each of which is a unique view of the hypercube as illustrated in Fig. 5. In this schematic, a spatially uniform illumination source that fills the entire field stop is shown. The illumination source is comprised of six infinitesimally narrowband monochromatic elements of equal intensity that are uniformly spaced in wavelength. A traditional image of the scene is formed at $(m_x, m_y) = \{(-1, -1), (-1, 0), (-1, 1), (0, -1), (0, 1), (1, -1), (1, 0), (1, 1)\}$, all of which contain spatiospectral information.

Tomographic methods are used to reconstruct a three-dimensional object from a series of two-dimensional images. In the CTIS image, the scene is the hypercube, which has three dimensions: two spatial dimensions (x, y) and one spectral dimension (λ) . Imaging of multiple sub-images of the hypercube in a single image enables the tomographic reconstruction of the datacube. Numerous sub-image patterns have been investigated, including linear and non-linear diffractions [6]; however the 3×3 array is the most common.

The CTIS image ${\bf g}$ can be mathematically represented as

$$\mathbf{g} = \mathbf{H} \mathbf{f} (x, y, \lambda) \tag{7}$$

where **H** is the system matrix which describes the geometric and spectral relationship between each sub-image such that a tomographic reconstruction can be performed; and $\mathbf{f}(x, y, \lambda)$ is the object (hypercube) being imaged. **H** is generally non-invertible, thus an estimation of the hypercube $\hat{\mathbf{f}}(x, y, \lambda)$ is required [18].

The system matrix \mathbf{H} is a sparse $N \times M$ matrix where N is the number of pixels in the entire CTIS image and M is the number of pixels in the (0,0) sub-image multiplied by the number of spectral bands (z) in the hypercube. For each pixel in the (0,0) sub-image, \mathbf{H} describes the locations where this pixel may be captured in the diffracted sub-images. The system matrix can be thought of as an $x \times y$ stack of matrices of the size a CTIS image. For this interpretation, each layer of the stack describes where the pixel in the (0,0) sub-image is captured in the other sub-images for each spectral band; with this three-dimensional stack reformatted into a two-dimensional matrix to suit Eq. (7). Additionally, the system matrix must also include the spectral response of the instrument at each wavelength for each sub-image. Neglecting to include the spectral response of the instrument in the system matrix may result in a reconstructed hypercube with significant

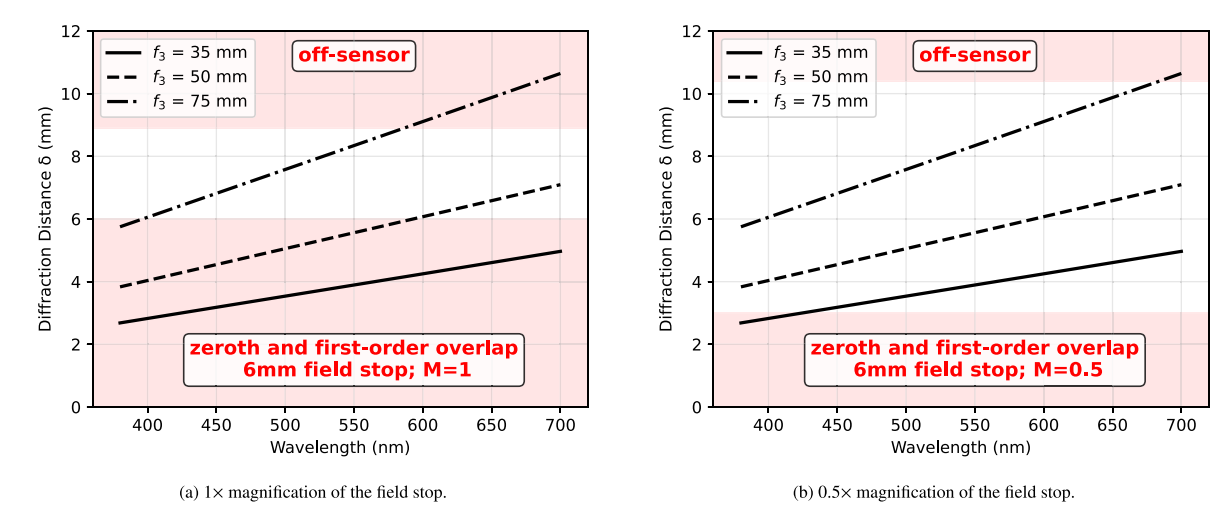


Fig. 4. Distance between the zeroth and first-order diffraction from the DE804 DOE for different re-imaging lens focal lengths. The line extents represent the sensitivity band of the sensor.

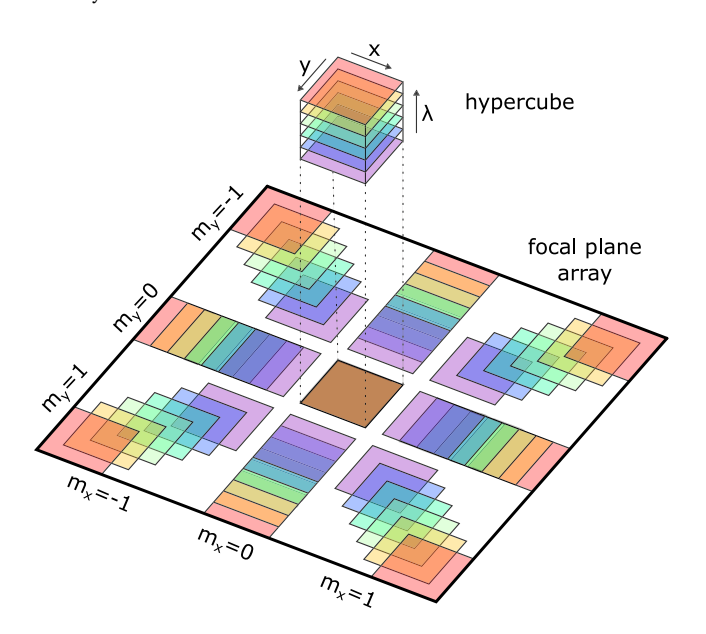


Fig. 5. Schematic representation of how the hypercube is imaged on the focal plane array as the CTIS image.

errors when the instrument response is not flat. These geometric and spectral response relationships are shown in Fig. 6 for a small example CTIS system. The system matrix developed in this work is of size $980\,100\times5\,269\,040$ with nonzero elements accounting for 0.000689% of the matrix.

A full experimental construction of the system matrix requires a spatial and spectral scan for all (0,0) sub-image pixels and all wavelengths in the hypercube, which is impractical. Instead, by invoking a spatial shift-invariance assumption where a spatial shift in the (0,0) sub-image results only in a spatial shift in the same direction in the other sub-images, the system matrix can be constructed efficiently [23]. Previously this has been achieved by using a monochromator to scan the wavelength of a monochromatic light source, requiring a large number of images to be captured. A similar, but alternate approach has been developed in this work, which is presented in Section 3.4.

There are a number of methods for solving the inverse problem of reconstructing the hypercube from the CTIS image (Eq. (7)) that are based on: (1) iterative approaches such as expectation maximisation (EM) and multiplicative algebraic reconstruction technique (MART);

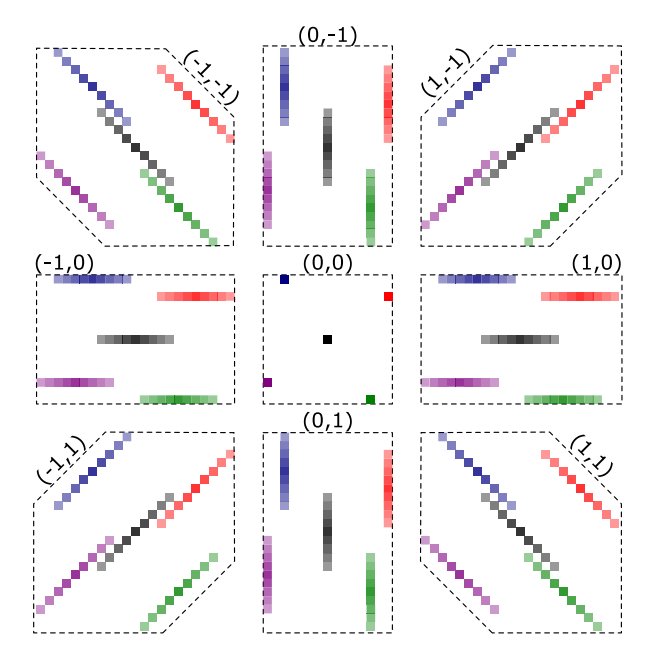


Fig. 6. Schematic representation of the reformatted system matrix for a limited selection of (0,0) pixels. In this schematic, a 15×15 pixel (0,0) subimage is shown with 9 spectral channels. Five points of the (0,0) sub-image are shown with different colours. These points selected to have non-overlapping first-order diffractions. The opacity of the diffracted elements represents the spectral response, which is assumed to be shift-invariant and equal for all orders in this schematic.

or (2) machine learning. Iterative approaches are typically used for CTIS reconstruction, due to their fast convergence and ease of implementation [7]. Convolutional neural networks (CNN) have been used to reconstruct CTIS images [22], however these methods require a large number of training images of similar scenes — data which are not available for re-entry demise events. A combined CNN and EM approach has been proposed [18] that enables the use of CNN models on dissimilar scenes and for high-noise data. In this work, the EM method was used to reconstruct the hypercube from the CTIS image. EM tends to converge rapidly, however high-frequency spatial and spectral artefacts can be introduced, typically at the edges of the hypercube [24], thus suitable convergence criteria must be used.

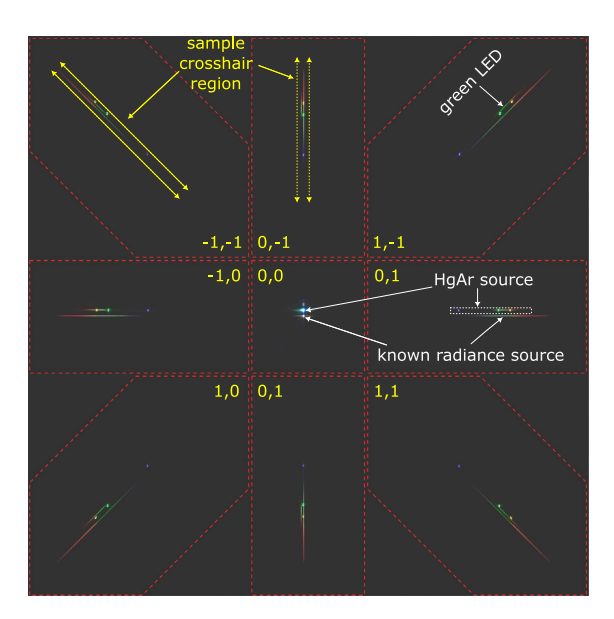


Fig. 7. Sample calibration image with both calibration lamps on. Spectral subimage (0,0) is partially saturated for clarity of the other orders. Note that true calibration images are analysed per colour channel and with one calibration lamp at a time.

To reconstruct $\mathbf{f}(x, y, \lambda)$ the expectation maximisation (EM) method per

$$\hat{f}_n^{k+1} = \frac{\hat{f}_n^{(k)}}{\sum_m H_{mn}} \sum_{m=1}^M H_{nm}^{\mathrm{T}} \frac{g_m}{\left(\mathbf{H}\hat{\mathbf{f}}^{(k)}\right)_m}$$
(8)

where \hat{f} represents an estimate of the hypercube [6]. In this work, the initial estimate $\hat{f}^{(0)}$ was set to one for all elements of the hypercube. The convergence of the EM algorithm for CTIS is typically monitored using image-level metrics such as mean-square error (MSE), peak signal-to-noise ratio (PSNR), or structural similarity index measure (SSIM). For a hypercube dominated by zero-intensity values, these metrics are not suitable as they do not provide a meaningful measure of convergence. Instead, the convergence of the EM algorithm in this work is monitored by the convergence of the reconstructed spectra for bright objects in the zeroth-order image.

3.4. Instrument calibration

3.4.1. Calibration setup

In this work, a new CTIS calibration method is used, based on existing calibration methods used in imaging spectroscopy. Instead of using a monochromator to scan known bandpasses of a known radiance source, this calibration method uses two calibration sources: (1) a wavelength identification source, and (2) a radiometric calibration source. The method is similar to the methods used in airborne reentry imaging campaigns [25], but does not have a strict co-location requirement for the two light sources. Further, there is no need for simultaneous imaging of the two light sources. A sample calibration image with both light sources on is shown in Fig. 7.

A calibration is also required to identify the geometric extents of the (0,0) sub-image. This is readily achieved by flooding the sensor with broadband light such that the (0,0) sub-image is saturated. This step is essential to fully describing the geometry of the CTIS image.

3.4.2. Wavelength calibration

The wavelength calibration process has two outputs: (1) a mathematical relationship that describes the distance of the diffracted image

from its source; and (2) the determination of $\lambda=f(z)$. The determination of $\lambda=f(z)$ can be used to correct for misalignment in the optical system; for example if the DOE and sensor axes are not perfectly aligned. This correction can be through image rotation or revision of the vector displacement detail in the system matrix. The wavelength identification source used in this work is an AVANTES AvaLight Hg lamp, which produces a number of narrowband spectral lines in the visible spectrum that can be imaged by the prototype (435.84 nm, 546.07 nm, 576.96 nm and 579.07 nm). These spectral lines are the high-intensity points in each diffracted sub-image of Fig. 7. Note that light from a green LED is included in the image — this is from the Hg lamp box and had no impact on the calibration process.

The DOE used behaves as a 2-D transmission grating at approximately $204\,\mathrm{lines\,mm^{-1}}$, therefore, in the visible spectrum, a linear relationship between the hypercube index z and wavelength λ is expected. This also implies that the distance $(\Delta x, \Delta y)$ from the light source in the (0,0) sub-image to any wavelength in the other sub-images also follows a linear relationship. As expected, $\Delta x = \Delta y$ was confirmed, so is hereafter simplified to Δ .

To identify the mathematical relationship that describes the distance of the diffracted image from its source, eight lines centred at the light source in the (0,0) sub-image were drawn at increments of 45° to pass through each diffracted sub-image of the light source. These were offset by two pixels in each direction to fully enclose the diffracted sub-images of the lamp; two of which are identified in Fig. 7 as the sample crosshair region. The eight extracted line spectra were extracted to identify $\lambda = f(\Delta)$ via linear regression. This step is important for the radiance calibration process as it is used to determine the sensitivity of each wavelength in the diffracted sub-images independent of an inverse analysis.

To determine $\lambda = f(z)$, the calibration image was processed using the EM algorithm to reconstruct the hypercube, thereby creating a line spectrum for the Hg lamp. For this wavelength identification calibration, the image is a simple point, where the amplitude of the spectrum is unimportant. Thus, for $\lambda = f(z)$ identification, the system matrix **H** used an efficiency value of one for all wavelengths. From the reconstructed Hg spectrum, $\lambda = f(z)$ was identified and confirmed to result in the same gradient (1.61 nm pixel⁻¹) as $\lambda = f(\Delta)$.

3.4.3. Radiometric calibration

For the radiometric calibration, a known radiance source was mounted in an integrating sphere. Calibrations were completed for a sweep of camera exposure times using a 1 mm and 2.4 mm diameter integrating sphere aperture. The background intensity of the CTIS image was assumed to be well-represented by a constant value, which was assumed to be the average of the pixel intensity values outside the sub-images. This background intensity value was subtracted from the CTIS image prior to the radiometric calibration analysis. The eight diffracted images of this radiance source were extracted from the CTIS image per the identification of $\lambda = f(\Delta)$ in Section 3.4.2, and reviewed to ensure there was no underlying amplitude offset from stray laboratory lighting or inappropriate background subtraction. The known $\lambda = f(\Delta)$ function was used to transform the pixel index of each diffracted image to wavelength.

Rather than completing a full calibration for each camera exposure and gain (ISO) setting which may be used, these camera changes were assumed to change only the amplitude of the sensitivity curve of the instrument per

$$S_{i,j}(\lambda) = C \times \hat{S}_{i,j}(\lambda) \tag{9}$$

where $S_{i,j}$ is the sensitivity of the instrument for sub-image (i,j); $\hat{S}_{i,j}$ is the sensitivity of the (i,j) sub-image normalised by the peak value of S in the set of diffracted sub-images; and C is a scalar multiplier that describes the change in sensitivity due to the exposure and gain settings. The validity of the scalar C assumption was confirmed by combining normalised line spectra from a sweep of camera settings

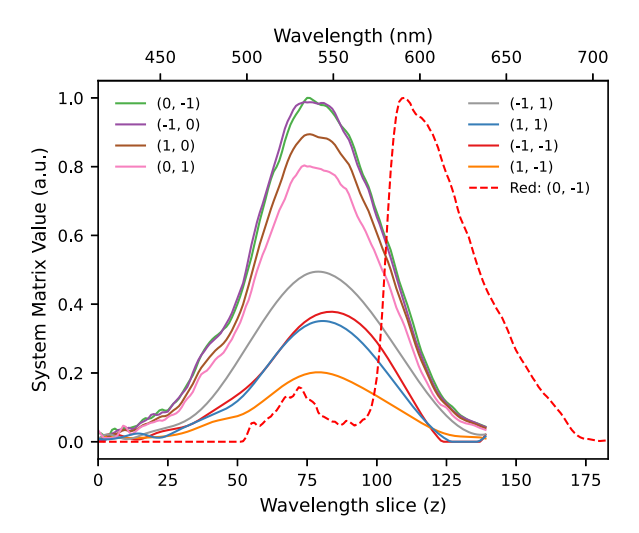


Fig. 8. Normalised spectral sensitivity of the green channel of the prototype instrument, shown as a function of the hypercube index z and wavelength λ . The green channel hypercube has a resolution of: $x=194;\ y=194;\ z=140.$ The red channel $\hat{S}_{0,-1}$ is presented for later reference.

to determine $\hat{S}_{i,j}(\lambda)$. Identification of C can be readily achieved for a particular camera setting and applied as a scalar multiplier to the system matrix \mathbf{H} . The normalised sensitivity calibration $\hat{S}_{i,j}(\lambda)$ is shown in Fig. 8 for the green channel of the prototype instrument. The sensitivity curves are dominated by the colour filter array (CFA) of the sensor—a monochrome sensor will result in a flatter sensitivity curve and be more suited to CTIS. As the sensitivity curves are dominated by the CFA, later figures in this work include $\hat{S}(0,-1)$ as a qualitative reference of instrument sensitivity.

Similar to previous calibration methods, the radiometric calibration is based on the spatial shift-invariance assumption and therefore is only required for a single point. Where multiple field stops are available, the system matrix as determined from the largest field stop can used for other field stops. This does increase computational time in the EM reconstruction, however, in this application there are no requirements for real- or near-real-time processing. Such versatility is advantageous for a re-entry demise application where there may be late changes to viewing geometry, such as a change in flight plan for airborne platforms due to weather or other operational constraints. Further, the absolute calibration is a function of the combination of sub-images used for the reconstruction. Should a particular sub-image require omitting due to saturation, the existing system matrix can be modified, with a new scalar *C* readily determined from existing calibration images.

One limitation of the radiometric calibration method presented is that does not identify $\hat{S}_{0,0}.$ Because the application is a sparsely populated field of point sources, the zeroth-order image reaches saturation at these points when the diffracted sub-images are far from saturation. To maximise the dynamic range of the instrument, the (0,0) sub-image is permitted to be saturated and therefore the radiometric calibration is not critical for the zeroth-order image. Should $\hat{S}(0,0)$ be required, a set of calibration images with narrow bandpass filters ahead of calibration source could be used to identify the zeroth-order sensitivity relative to the other sub-images. If the (0,0) sub-image must not be saturated at any point, a neutral density (ND) filter covering only the (0,0) region of the sensor could be implemented. A ND filter for the (±1, 0) subimages may also be beneficial should the CTIS x axis be aligned with the long axis of the debris field. In the present study, the efficiency of the (0,0) sub-image was assumed to follow the sensor spectral response curve. While there will be effects from the DOE, since the sub-image is saturated, the true spectral response of the (0,0) sub-image is not critical for the present study.

In this work, the system matrix **H** does not include a point spread function (PSF) of the instrument. This could be implemented in a future design, however the viability of the CTIS instrument for re-entry demise measurements can be demonstrated without the inclusion of a PSF.

4. Capability demonstration

4.1. Experimental setup

To investigate the feasibility of using a CTIS instrument for re-entry demise measurements, the prototype instrument was used to measure test scenes that contains similar spatiospectral features to those expected in a re-entry demise event. Therefore, the laboratory-based test scenes were designed to contain point sources with high-frequency spatial and spectral features to approximate the image elements of a re-entry demise event.

A test scene was constructed using three light sources: (1) a known radiance continuum point source; (2) a Hg lamp; and (3) a fluorescent tube positioned behind an optical breadboard to form point sources. The known radiance point source provided a method for investigating the spectral irradiance reconstruction capabilities of the CTIS instrument, while the other lamps contain high-frequency spectral features. The use of the fluorescent tube added significant spatiospectral complexity to the scene.

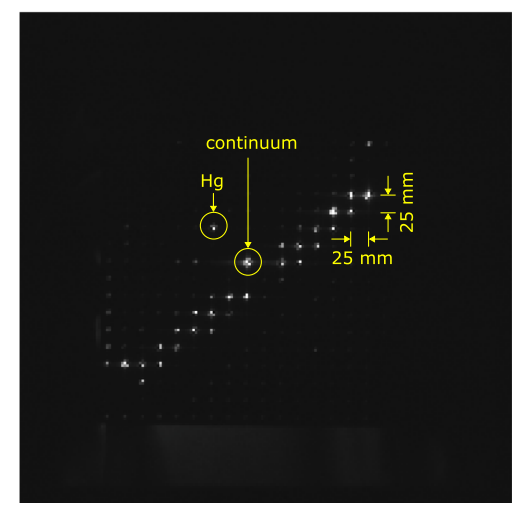
To achieve a sparsely populated scene of point sources, an optical breadboard with 25 mm pitch was placed immediately in front of these light sources. The M6 holes of the breadboard were too large for a suitable aperture, therefore 3D-printed inserts with 2 mm diameter clear apertures were threaded into the M6 holes. No effort was made to achieve a similar intensity for each fluorescent tube point source — the accuracy of the spectral irradiance reconstruction could be assessed from the known radiance point source. The resulting test scene is shown in Fig. 9(a), as imaged on the green channel of the instrument as the (0,0) sub-image.

The axes of the rectangular hole pattern of the optical breadboard was approximately aligned with the x and y axes of the CTIS instrument. This ensured overlap of the point sources in the orthogonal first-order sub-images as shown in Fig. 9(b). Additionally, because the breadboard holes are also aligned along a 45° angle, the non-orthogonal sub-images have significant spectral overlap, especially for the $(\pm 1, \mp 1)$ sub-images. For the $\pm (1,1)$ sub-images, the Hg lamp overlaps only with low intensity fluorescent tube points and the continuum lamp due to the mechanical housings of each light source. Priority was given to ensuring that there was no sub-image where the diffraction from the known radiance signal was present without overlap from at least one other point source.

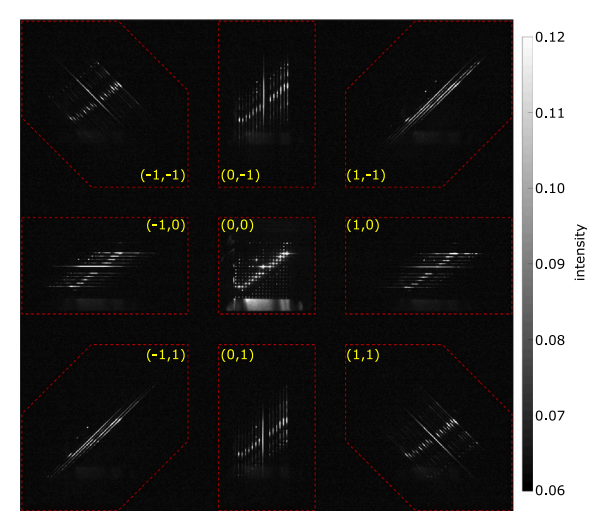
Two test scenes were analysed: (A) a simplified case where only a known radiance point source was present; and (B) the scene shown in Fig. 9 where the known radiance point source, a Hg lamp and fluorescent tube point sources were present. The value of Case (A) is that it provides a simple scene for investigating: (1) the spectral irradiance reconstruction capabilities of the CTIS instrument; and (2) a study of the required signal amplitude for accurate spectral radiance reconstruction of a simple scene. The latter is important as multiple point sources will overlap, therefore the available dynamic range for a particular point source is reduced relative to what is available for a single point source.

4.2. Case (A): Spectral irradiance of a single point source

The performance of the prototype CTIS instrument for reconstructing the spectral irradiance of a single known radiance point source is shown in Fig. 10. The simplest scene for a CTIS reconstruction is a single point source [6], and as expected the spectral irradiance reconstruction is accurate for this case. As shown in Fig. 10(a), there is an increase in reconstruction noise at the edges of the wavelength

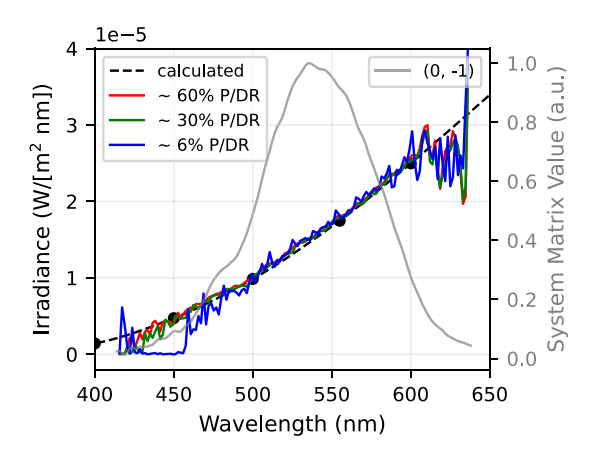


(a) Sub-image of the (0,0) order of resolution 194×194 pixels.

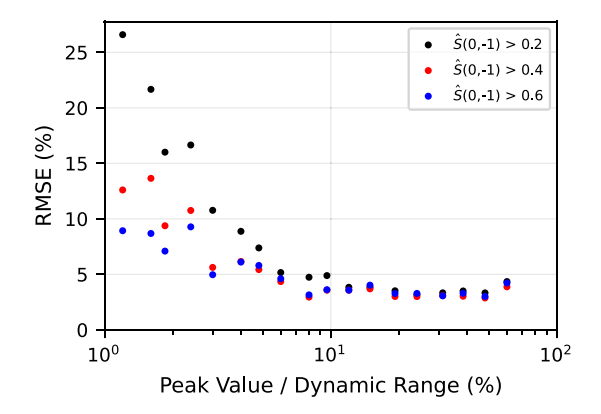


(b) CTIS image with sub-images identified.

Fig. 9. CTIS image for case (B) of the test scene as extracted from the green channel of the camera. Unidentified sources in (a) are the fluorescent tube point sources. The (0,0) sub-image is saturated at full-image colourscale, thus there are stray light artefacts present in this sub-image.



(a) CTIS spectrum reconstruction of the known radiance point source for different peak signal intensities.



(b) Root-mean-square error (RMSE) of the reconstructed spectra.

Fig. 10. CTIS results for test case (A): a single known radiance point source.

range presented. While increased noise at the edge of a CTIS hypercube is expected, the noise in this case is likely dominated by the low-sensitivity of the sensor at these wavelengths. For the 6% P/DR case, there is a change to the noise in the reconstructed spectrum at around 450 nm compared to the other cases. This is attributed to the low signal amplitude and low sensitivity of the sensor at this wavelength, the combination of which has resulted in the irradiance not being discernable from the background intensity in this wavelength region.

To investigate the ability of the instrument to reconstruct point sources of different intensities, the exposure time of the camera was varied to change the amplitude of the measured first-order diffractions. Since the maximum pixel intensity is proportional to the exposure time, the peak signal divided by the dynamic range (P/DR) used for the point source was varied. In Fig. 10(a), it is clear that the noise in the reconstructed spectrum is greatest at the low-sensitivity edges of the sensor. To compare the accuracy of the reconstructed spectra with signal amplitude, the root-mean-square error (RMSE) of the reconstructed spectra was calculated for different $\hat{S}(0,-1)$ cutoffs as presented in Fig. 10(b). The RMSE has a floor of approximately 2.8%, which indicates a tendency for the spectral irradiance to be overestimated in this test case. This can be attributed to a systematic error in the calibration and alignment of the instrument, with potential

impacts from the low-sensitivity edges of the sensor. For the sensitivity bands presented, there is minimal change in the RMSE when the peak intensity of the diffracted sub-images is above approximately 6% of the dynamic range of the sensor. This demonstrates that the CTIS technique can accurately reconstruct signals of low amplitude for a simple field, which is important for application to complex fields with overlapping diffracted spectra. However, this conclusion must be revisited through measurements of more complex scenes, such as case (B).

4.3. Case (B): Spectral irradiance of an array of point sources

4.3.1. Convergence monitoring

As an iterative approach (EM) was used to reconstruct the hypercube, it is important to monitor the convergence of the algorithm so not to over-iterate and introduce high-frequency artefacts to the hypercube. Fig. 9 shows that the (0,0) sub-image is sparsely populated in space and in wavelength, therefore the hypercube is dominated by zero-intensity values. Image-level convergence metrics such as IMSE, SSIM and PSNR compare two images, in this case the image generated at iteration k+1 with the image generated at iteration k. With a sparsely populated hypercube, these metrics are not suitable as they do not provide a meaningful measure of convergence. Instead, convergence of the EM

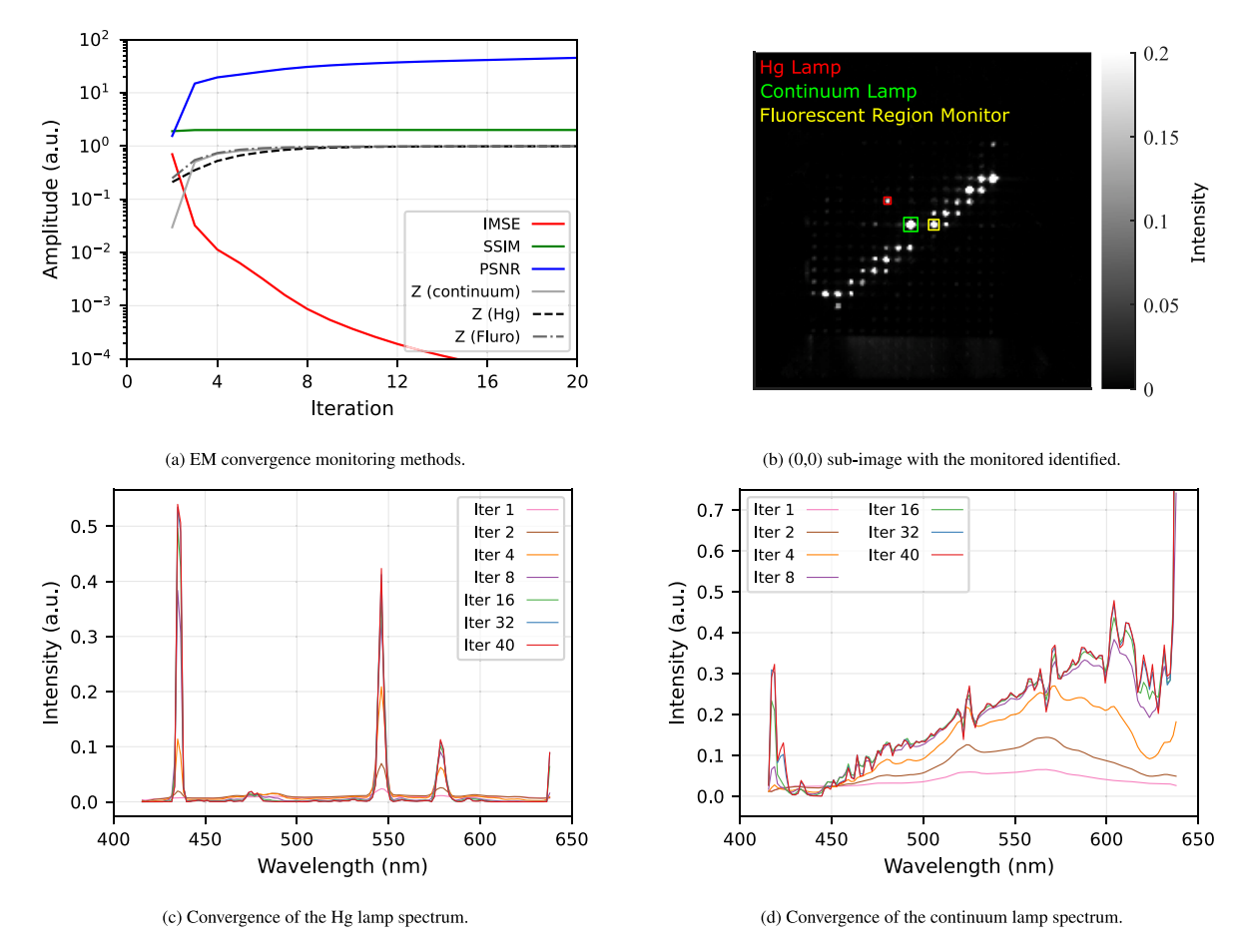


Fig. 11. Spectral reconstruction of the multiple point source scene.

algorithm can be monitored by reporting the reconstructed spectra for bright objects. Here, the convergence Z for a defined region is defined as:

$$Z = 1 - \frac{\left\| \hat{I}_{k+1} - \hat{I}_{k} \right\|}{\left\| \hat{I}_{k} \right\|} \tag{10}$$

where \hat{I} is the reconstructed spectrum for the region of interest.

The convergence metric comparison is demonstrated in Fig. 11(a), where the image-level and region-level convergence metrics are shown for test case (B). The regions of interest are shown on the (0,0) subimage in Fig. 11(b). From Eq. (10), the SSIM is not useful for this application and, while the PSNR and IMSE do provide some insight, they do not asymptote to a value within the number of iterations shown, nor does a clear 'converged' amplitude criteria emerge that could be applied to different scenes. Instead, by monitoring the spectrum for a specific region, the convergence metric Z can be used to determine when the EM algorithm has converged.

From Eq. (10), all monitored regions are shown to converge to a stable amplitude after about 12 iterations. As a valuable check, it is important to analyse the reconstructed spectra in Figs. 11(c) and 11(d) to ensure that the convergence metric Z is not misleading like the image-level metrics. Within a few iterations, the line emissions of the Hg lamp are clearly visible, converging to a stable amplitude between 16 and 32 iterations. The convergence of the continuum lamp spectrum also shows convergence in the same number of iterations. The accuracy of the spectral reconstruction from this test case is discussed in Section 4.3.2, however it is clear that there is high noise at the edges of the wavelength range like in case (A).

4.3.2. Spectral reconstruction performance

The spectral reconstruction performance of the CTIS instrument for the multi-point scene was assessed by: (1) investigating its ability to reconstruct line emissions; and (2) the ability to accurately reconstruct the measured spectral irradiance of a known radiance point source from the complex scene of case (B). The line emission metric was completed for the Hg and fluorescent tube sources as these contain high-frequency spectral features, while the known radiance point source was used to assess the spectral irradiance reconstruction performance.

Fig. 12 shows the spectral reconstruction of the Hg lamp and fluorescent tube. These plots include a normalised intensity reference spectrum for both lamps, which were measured using a Thorlabs CCS175 compact spectrometer, which has an operating bandpass of 500 nm to 1000 nm. A non-dimensional wavelength sensitivity calibration was completed for the Thorlabs spectrometer to correct for the instrument response of this spectrometer. There are CTIS data below 500 nm, but the data within the Thorlabs spectrometer operating range is sufficient to assess the spectral reconstruction performance.

While there are four Hg lines present in Fig. 12(a), only three were identified by CTIS. This is the result of the instrument dispersion, which is approximately 1.6 nm pixel⁻¹ for the green channel, so the lines separated by 2.1 nm cannot be independently resolved. There is broadening of the Hg lines which can be resolved individually by the CTIS measurement at 435.84 nm and 546.07 nm. The FWHM of the CTIS reconstruction is approximately 3.2 nm at 435.84 nm and 3.8 nm at 546.07 nm, the latter of which has a FWHM of approximately 0.85 nm when measured by the Thorlabs spectrometer. This 3.2 nm to 3.8 nm FWHM is of the order of two times the design dispersion of the CTIS instrument. With two datapoints for the FWHM, it is not feasible to determine if the instrument broadening is constant or a function of

wavelength; however, it is likely a function of wavelength resulting from chromatic aberrations in the optical system and the increasing impact of the off axis effects with increasing wavelength. Despite the instrument broadening, the Hg lines were reasonably well wavelength resolved, with improvements to the wavelength resolution likely to improve the resolution of the Hg lines. The CTIS reconstruction was able to resolve the zero-intensity regions between the Hg lines, which is important for the spectral reconstruction of a complex scene.

The line widths from the Hg lamp are significantly narrower than can be resolved by the prototype CTIS instrument. Broader line widths were available from the fluorescent tube, which has a number of broad emissions (Fig. 12(b)) from phosphors and two line emissions from the mercury vapour used to fluoresce the phosphors. The line width at around 546 nm is 8.3 nm FWHM for CTIS and 5.3 nm FWHM for the Thorlabs spectra. This is a factor of approximately 1.6 increase in the FWHM of the CTIS reconstruction relative to the Thorlabs spectrometer for this region, with CTIS instrument broadening at 612 nm a factor of approximately two.

In Fig. 12(b), two Thorlabs spectra with different scaling are presented to better describe the spectral features of the fluorescent tube. This was required as the high-resolution Thorlabs spectrometer sample resolution is $0.155\,\mathrm{nm\,pixel^{-1}}$, approximately 10 times finer than the CTIS instrument, thus the Thorlabs spectrometer was able to resolve the narrow spectral features of the fluorescent tube. For example, the Thorlabs spectrometer identified the 612 nm line with a peak intensity approximately 44 times the peak intensity at 588 nm. For a lower spectral resolution, such as the CTIS instrument, the narrow high-intensity spectral features are broadened and the peak intensity is reduced.

In Fig. 12(b), the green channel of the CTIS instrument was unable to identify separate peaks for the lines at 542.7 nm and 546.9 nm, which are separated by 4.2 nm. While in a low sensitivity wavelength for the red channel, there is an indication of two peaks in the red channel and reduced broadening of the spectrum relative to the green channel. This can be traced to how the data was collected on the RGGB CFA and later reformatted to three colour channels. For an individual RGGB pixel, the extracted green image is the average of the two green pixels, which introduces broadening of the spectral features. Because there is not a suitable wavelength range where both the green and red channels both have high sensitivity (see Fig. 8), a quantitative comparison of the irradiance measured using these individual channels was not completed.

In the $570\,\mathrm{nm}$ to $620\,\mathrm{nm}$ band, both the complex spectral features of the fluorescent tube were partially resolved by the CTIS instrument. The $612\,\mathrm{nm}$ emission was separated from the lower intensity emissions between $576\,\mathrm{nm}$ and $606\,\mathrm{nm}$, and between $620\,\mathrm{nm}$ and $634\,\mathrm{nm}$. However, individual peaks within these lower-intensity regions could not be individually resolved. This is affected by the instrument resolution possibly the low relative intensity of these spectral features.

Like the Hg lamp reconstruction, the zero-intensity regions between the spectral features were resolved. Overall, the CTIS instrument was able to resolve the high-intensity high-frequency spectral features of the Hg lamp and fluorescent tube; however, increasing the wavelength resolution of the instrument should be considered for practical use in re-entry demise measurements. A factor of 1.5 increase in wavelength resolution is possible with the current design by changing only the DOE, thereby not affecting the present spatial field of view. Removing the CFA from this sensor would provide a further 2× increase in both wavelength and spatial resolution; and provide an unquantified sensitivity improvement.

The accuracy of the spectral irradiance reconstruction was assessed using the known radiance point source that was analysed as a single object scene in Section 4.2. As the multi-point scene contained significant spectral overlap, the peak magnitude of this point source was equivalent to the 12% dynamic range of the sensor case from Section 4.2. The results of the case (B) spectral reconstruction are shown in Fig. 13. Consistent with Fig. 10(a), there is an increase in noise at the

edges of the wavelength range. The CTIS reconstruction also follows the calculated spectral irradiance, however there are reconstruction errors at approximately 525 nm and 570 nm. These wavelengths are close to the peak efficiency for all sub-images, so these errors were unexpected and were not present in the single-point source case. A review of the convergence showed that these errors were present immediately following the initial guess of a uniform hypercube. Therefore, these errors are either a result of a systematic error in the system matrix (such as the omission of a PSF), or a limitation of the CTIS method for this scene. It is also possible that alternative reconstruction methods, such as a combined iterative-CNN approach, may be more suitable for this scene. Nonetheless, the low-frequency and amplitude match of the CTIS reconstruction to the calculated spectrum demonstrates potential of the CTIS method for re-entry demise measurements.

A potential application of the CTIS instrument to re-entry demise is the generation of filtered images of custom and selectable bandpasses; bandpasses which can be adjusted to target specific spectral features of interest. While the image resolution is less than that for a dedicated filtered imager, significantly more data is captured using CTIS than from one single filtered imager. This is especially important for airborne platforms where window space is limited. Three CTISgenerated bandpass filtered images of the test scene are shown in Fig. 14. To generate these bandpass images, the hypercube was linearly interpolated at the bandpass edges, and the bandpass filter assumed to be ideal. The selected bandpass filters were chosen to be 10 nm wide in this demonstration to approximate a 10 nm FWHM bandpass filter; a commonly available option. Bandpasses were centred at 546 nm (Fig. 14(a)), 565 nm (Fig. 14(b)) and 577 nm (Fig. 14(c)) to target bandpasses with and without significant energy from the Hg lamp and fluorescent tube. Comparison of CTIS-generated bandpass filtered images to images captured using physical bandpass filtered images is an avenue for instrument validation of: (1) re-entry observations; (2) measurements in the related fields of shock tunnels and plasma facilities; and (3) generalised applications of CTIS.

5. Discussion

5.1. Prototype revisions for a CTIS system to image re-entry demise events

While the prototype CTIS instrument has demonstrated the feasibility of using a CTIS instrument for re-entry demise measurements, there are revisions that must be made to this prototype to make it practical for re-entry demise measurements; many of which are improvements that are true for all CTIS systems. The greatest limitation of the prototype instrument is the DOE. Its aperture is too small, which results in approximately 92% of the light that reaches the DOE not being diffracted into the sub-images. Increasing the aperture of the DOE will increase the light throughput and therefore the sensitivity of the instrument. The DOE used in the prototype generates a 5×5 array of sub-images, with the centre 3 × 3 being used. Diffracting unused sub-images reduces the useful light throughput, therefore a DOE which generates only the required sub-image pattern should be used. The third change to the DOE is its diffraction angles should be increased to make full use of the sensor area. Increasing to an equivalent of 300 lines mm⁻¹ would make full use of the short axis of the sensor and increase the wavelength resolution by a factor of approximately 1.5. Implementing a DOE that produces a rectangular pattern rather than a square pattern would enable using the long axis of the sensor. Hexagonal diffraction patterns may also be advantageous as they can provide a more efficient packing of sub-images on the sensor. Because spatial resolution is important for re-entry demise measurements, it is unlikely that other diffraction patterns with a larger CTIS image fill factor, such as radial patterns [6], are feasible. Further, increasing the diffraction angle can facilitate the use of larger field stops with the $0.5\times$ magnification of the prototype; or a 1.0× magnification for smaller field stop without a significant reduction of the spatial field of view.

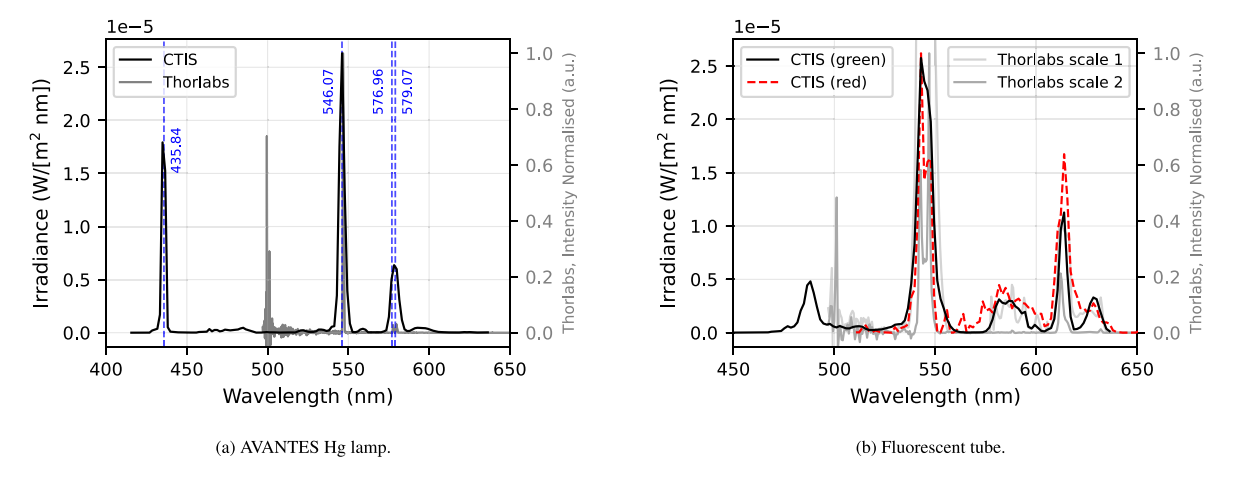


Fig. 12. Spectral reconstruction of the line-source lights. See Fig. 11(b) for the location of the regions reported in this figure.

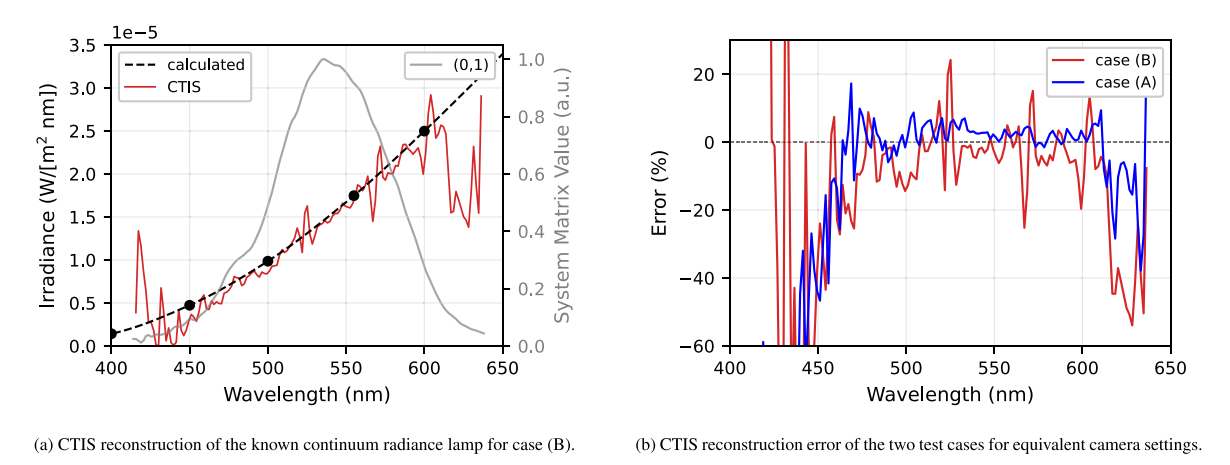


Fig. 13. CTIS reconstruction of the known radiance source.

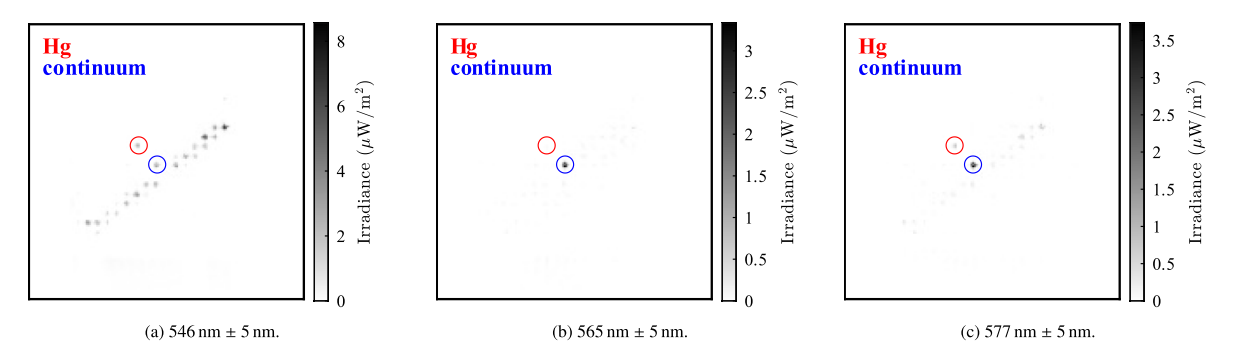


Fig. 14. CTIS-generated bandpass filtered images of the case (B) test scene.

The sensor used for a practical system should utilise a monochrome sensor rather than a colour filter array sensor. This will increase the sensitivity of the instrument and broaden the spectral response of the instrument. Ideally, this sensor is a scientific-grade sensor that can be programmed to change the exposure time and gain settings to make full use of the sensor dynamic range without saturation. Because the CTIS image is complex and contains significant spectral overlap, it is difficult to predict suitable exposure and gain settings. While saturation of the diffracted sub-images should be avoided, Section 5.2 discusses the feasibility of using a reduced system matrix to reconstruct the hypercube when some sub-images are saturated. The sensitivity improvements from DOE and sensor changes are essential for a practical CTIS system to be used for re-entry demise measurements where exposure times

longer than a few tens of milliseconds are impractical due to the dynamic properties of the scene. Since CTIS requires diffraction along a direction with a strong object relative velocity component, exposure times less than those used for traditional imaging spectroscopy are required. This maximum feasible exposure time is difficult to quantify as it depends on operational parameters such as the tracking system used and the re-entry trajectory relative to the observation platform. The sensor for a re-entry CTIS system should also utilise a global shutter so that the image accurately captures the scene for a single period of time.

Because the target scene is dominated by point sources, the (0,0) sub-image has a tendency to saturate. For the test scenes, this saturation was not a significant limitation; however it is recommended to

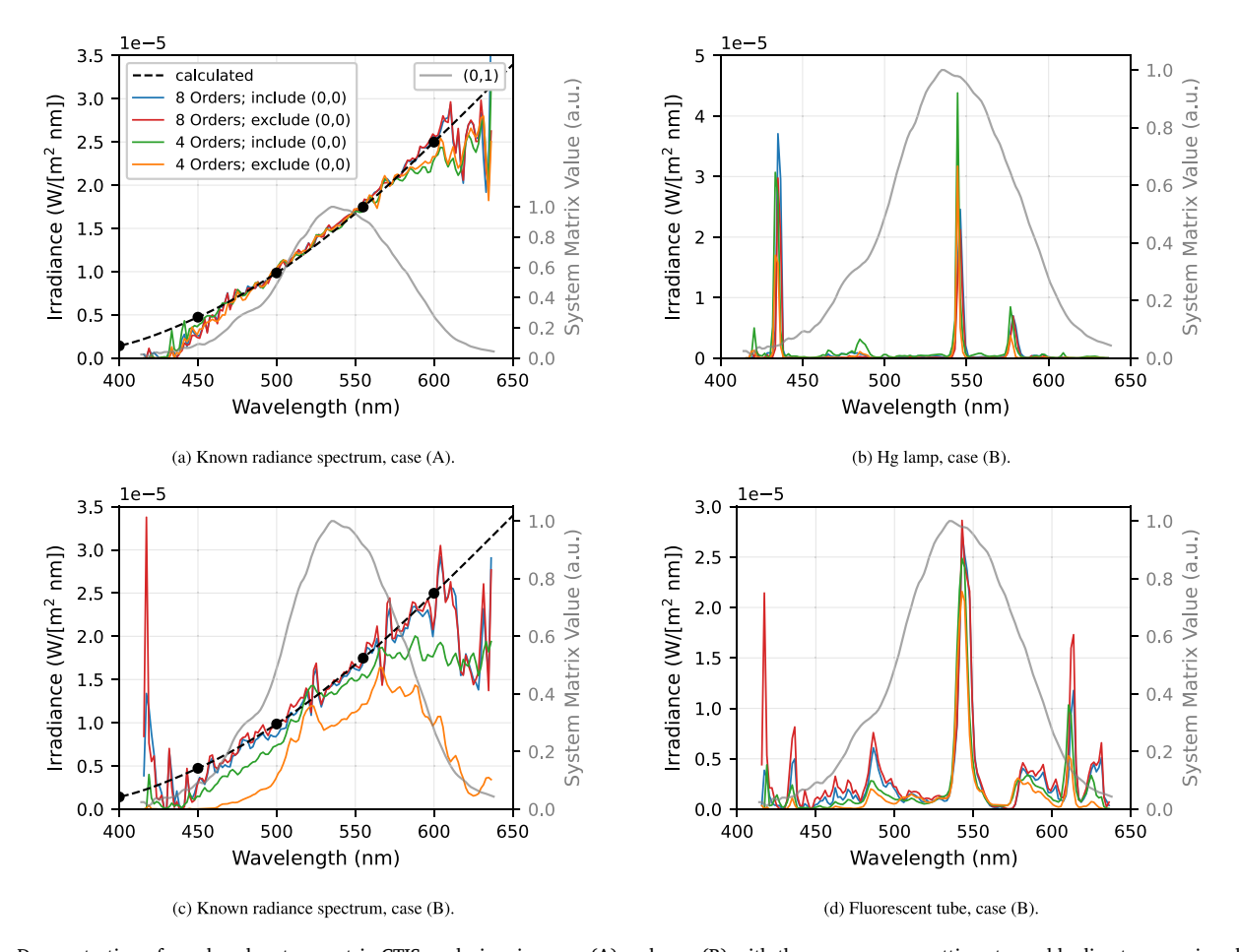


Fig. 15. Demonstration of a reduced system matrix CTIS analysis using case (A) and case (B) with the same camera settings to enable direct comparison between Figs. 15(a) and 15(c). The four orders included in the reduced system matrix are the orthogonally diffracted images: (0,1), (0,-1), (1,0), (-1,0).

implement a neutral density (ND) filter in the (0,0) region of the sensor to reduce the intensity of this sub-image. Implementation of spectral edgepass filters are recommended to limit the effects of low-efficiency wavelengths on the CTIS reconstruction. Edgepass filters can be used to limit the spectral sensitivity of the instrument to the wavelengths of interest, such as the NUV and blue wavelengths where many atomic metals emit during re-entry demise. Targeting these lower wavelengths can enable a higher diffraction angle DOE or longer focal length lens imaging lens to be used, thereby increasing the spectral resolution of the instrument for a fixed spatial resolution.

Finally, a thorough CTIS instrument design should have prior knowledge of the expected scene so a suitable field of view can be selected. Since the spatial field of view and the wavelength range of the CTIS instrument are coupled and inversely related, a thorough design investigation of suitable resolutions for all three axes of the hypercube is essential for maximising the quality of scientific data that can be collected.

5.2. Use of a reduced system matrix

In Section 4 the analysis has focused on using all eight first-order sub-images. Where there are multiple point sources, there is a risk that their overlapping dispersions will result in saturated data in the diffracted sub-images. A saturation may not occur in the diffracted image with the greatest efficiency—a saturation may occur in any sub-image depending on where the point sources are located in the (0,0) sub-image. For example, case (B) preferentially saturates the (1,-1) and (1,-1) sub-images due to the alignment of point sources along one diagonal of the (0,0) sub-image. Additionally, owing to the spacing and

spectral content, saturation of a sub-image does not necessarily result in saturation of the opposite sub-image. If a sub-image, or multiple sub-images are saturated, the frame may remain viable; a system matrix which omits these sub-images can be used to reconstruct the hypercube, albeit at a potential resolution penalty. The number of combinations of the potential eight diffracted sub-images of a 3×3 CTIS image can be used to build a system matrix is:

$$N = \sum_{n=m}^{8} \frac{8!}{n!(8-n)!} \tag{11}$$

where n is the number of sub-images used in the system matrix and m is the minimum number of sub-images required for a valid reconstruction. The minimum number of sub-images required depends on which sub-images are saturated and the scene being imaged. Nonetheless, should m=4, the number of potentially valid sub-image combinations is N=163. A parametric study of these combinations is not in the scope of this work, however it is an interesting direction should real re-entry data from a CTIS instrument be acquired.

In the context of a re-entry demise application, the debris field is long and narrow. If the CTIS x axis is aligned with the long axis of the debris field, then the $(\pm 1,0)$ sub-images are likely to be of significantly higher intensity than the other diffracted sub-images. This is similar to the preferential saturation of the $(\pm 1, \mp 1)$ sub-images in case (B).

A feasibility demonstration of using reduced system matrices is presented in Fig. 15 for four system matrices: (1) a complete hypercube reconstruction with all eight sub-images and the zeroth-order image known; (2) a reconstruction using the eight diffracted sub-images only; (3) a reconstruction with only the orthogonal sub-images and the zeroth-order image known; and (4) a reconstruction with only the non-orthogonal sub-images. The efficiency of the (0,0) order was assumed

to be the average of the orthogonal sub-images, thus largely following the sensor response curve. The shape of the (0,0) sensitivity is likely different due to the diffractive properties of the DOE, however, since the (0,0) sub-image is saturated, the exact shape of the sensitivity is not critical for this analysis. Omitting the (0,0) information from the reconstruction was used to assess if a CTIS system without any information from the (0,0) image could be feasible.

For the simple single point source in Fig. 15(a), the CTIS spectrum for all four system matrices follow the calculated irradiance spectrum. However, when the same spectrum is extracted from the complex scene of case (B) is considered, more differences between the results from the four system matrices are observed. When all eight diffracted subimages are used, the CTIS reconstruction did not require information from the (0,0) sub-image. When only the orthogonally diffracted subimages were used, the CTIS reconstruction of the continuum lamp followed the same shape as the calculated irradiance, but at a lower amplitude. For the four-order systems, the best amplitude match to the calculated irradiance is from 530 nm to 560 nm, where the system efficiency is highest. When excluding the (0,0) information from the four sub-image system, the CTIS reconstruction is poor in amplitude and shape. This suggests that the (0,0) sub-image (i.e. direct spatial information) becomes more important as the number of diffracted sub-images reduces.

The reduced system matrices presented in Fig. 15 were all able to capture the high-amplitude emissions from the Hg lamp (Fig. 15(b)) and fluorescent tube (Fig. 15(d)). Lower intensity emissions are not consistently reconstructed, such as at around $490\,\mathrm{nm}$ for the fluorescent tube. Despite the amplitude differences, the reduced system matrices presented could be applied to the identification of atomic lines and subsequently materials and objects in the re-entry demise field.

6. Conclusions

Through the reconstruction of a representative test scene measured using a prototype instrument, the computed tomographic imaging spectroscopy (CTIS) technique was demonstrated to be a promising technology for remote observation of re-entry demise events. The test scene was designed to include high-frequency spatial features and narrowband emissions to simulate the properties of a re-entry demise field; scene characteristics which have not previously been investigated using CTIS. The CTIS reconstruction of narrowband emissions successfully identified high-intensity spectral features with FWHM of the order of 1 nm, showing potential application to material and object identification in re-entry demise events. Lower intensity spectral features were not often not sufficiently spaced in wavelength to be resolved by the prototype CTIS instrument, however, where there was sufficient separation, the dynamic range was adequate for wavelength identification purposes. Reconstruction of a known continuum irradiance in a complex scene was moderately successful.

Recommendations for a practical CTIS system based on the prototype were made, with the primary limitations of the prototype being the diffractive optical element and the colour sensor. A novel CTIS calibration method was introduced that requires less manual interventions than previous methods, making it suitable for both field and laboratory calibrations. The convergence of the expectation-maximisation (EM) algorithm was monitored using a region-level convergence metric, which was shown to be more effective than image-level metrics for the sparsely populated hypercube.

In addition to the spectral reconstruction performance, bandpass filtered images were generated from the CTIS hypercube. Spectral measurements of individual objects within a re-entry debris field are yet to be achieved, this the motivation for this research. Validation of the CTIS technique for re-entry demise measurements is required, which, given the challenges of acquiring object-level spatiospectral resolution, is not trivial. However, the CTIS-generated bandpass filtered images show promise for use as a cross-instrument validation.

CRediT authorship contribution statement

Byrenn Birch: Writing – review & editing, Writing – original draft, Visualization, Validation, Software, Resources, Project administration, Methodology, Investigation, Funding acquisition, Formal analysis, Data curation, Conceptualization.

Declaration of competing interest

The authors declare that they have no known competing financial interests or personal relationships that could have appeared to influence the work reported in this paper.

Acknowledgements

Byrenn Birch is the recipient of an Australian Research Council Discovery Early Career Researcher Award (DE250100012) funded by the Australian Government. The open-sourcing of sample CTIS scripts from [18] is gratefully acknowledged for accelerating the development of the analysis code presented in this work. This work would not have been possible without the mentorship and support of David Buttsworth and Fabian Zander, especially their facilitation of re-entry observation opportunities.

References

- [1] J.H. Grinstead, P. Jenniskens, A.M. Cassell, J. Albers, M.W. Winter, Airborne observation of the hayabusa sample return capsule re-entry, in: 42nd AIAA Thermophysics Conference, 2011, pp. 1–11, http://dx.doi.org/10.2514/6.2011-2320
- [2] S. Löhle, R. Wernitz, G. Herdrich, M. Fertig, H.P. Röser, H. Ritter, Airborne re-entry observation experiment SLIT: UV spectroscopy during STARDUST and ATV1 re-entry, CEAS Space J. 1 (2011) 59–69, http://dx.doi.org/10.1007/ s12567-010-0005-3
- [3] B. Kraetzig, S. Löhle, D.R. Buttsworth, Evolution of plasma species and heatshield temperatures from hayabusa reentry observation, J. Spacecr. Rockets 51 (2014) 823–837, http://dx.doi.org/10.2514/1.A32854.
- [4] F. Zander, S. Löhle, A review of airborne observations for space debris re-entry break-up and dispersion measurements, CEAS Space J. (2025) http://dx.doi.org/ 10.1007/s12567-025-00608-9.
- [5] M. Boyda, C. Scott, H.J. Kim, K. Scott, NASA SCIFLI's Calibrated Mission Portfolio, Presentation, (20240006897) NASA Langley Research Center, Hampton, VA, USA, 2024, URL https://ntrs.nasa.gov/citations/20240006897.
- [6] N. Hagen, E. Dereniak, D. Sass, Maximizing the resolution of a CTIS instrument, in: S.S. Shen, P.E. Lewis (Eds.), Imaging Spectroscopy XI, International Society for Optics and Photonics, 2006, http://dx.doi.org/10.1117/12.680750.
- [7] C. Douarre, C.F. Crispim-Junior, A. Gelibert, G. Germain, L. Tougne, D. Rousseau, CTIS-net: A neural network architecture for compressed learning based on computed tomography imaging spectrometers, IEEE Trans. Comput. Imaging 7 (2021) 572–583, http://dx.doi.org/10.1109/TCI.2021.3083215.
- [8] E. Hege, D. O'Connell, W. Johnson, S. Basty, E. Dereniak, Hyperspectral imaging for astronomy and space surveillance, in: Proc. SPIE 5159, Imaging Spectrometry IX, International Society for Optics and Photonics, 2004, pp. 380 – 391, http: //dx.doi.org/10.1117/12.506426.
- [9] S. Löhle, T. Marynowski, A. Knapp, R. Wernitz, T. Lips, Analysis of the ATV1 re-entry using near-UV spectroscopic data from the ESA/NASA multi-instrument aircraft observation campaign, in: Proceedings of the 7th European Symposium on Aerothermodynamics for Space Vehicles (ESA SP-692), vol. 2011, 2011.
- [10] R. Ravichandran, B. Birch, A. Lock, D. Buttsworth, F. Zander, Hayabusa2 surface and shock layer radiation from the Australian airborne observation, J. Spacecr. Rockets 62 (4) (2025) 1377–1386, http://dx.doi.org/10.2514/1.A36225.
- [11] J.B. Snively, M.J. Taylor, P. Jenniskens, Airborne imaging and NIR spectroscopy of the ESA ATV spacecraft re-entry: Instrument design and preliminary data description, Int. J. Remote Sens. 32 (2011) 3019–3027, http://dx.doi.org/10. 1080/01431161.2010.541516.
- [12] S. Löhle, M. Eberhart, F. Zander, A. Meindl, R. Rudawska, D. Koschny, J. Zender, R. Dantowitz, P. Jenniskens, Extension of the plasma radiation database PARADE for the analysis of meteor spectra, Meteorit. Planet. Sci. 56 (2) (2021) 352–361, http://dx.doi.org/10.1111/maps.13622.
- [13] P. Jenniskens, J. Albers, M.W. Koop, M.S. Odeh, K. Al-Noimy, K. Al-Remeithi, K. Al Hasmi, R.F. Dantowitz, F. Gasdia, S. Löhle, F. Zander, T. Hermann, D. Farnocchia, S.R. Chesley, P.W. Chodas, R.S. Park, J.D. Giorgini, W.J. Gray, D.K. Robertson, T. Lips, Airborne observations of an asteroid entry for high fidelity modeling: Space debris object WT1190F, in: 54th AIAA Aerospace Sciences Meeting, 2016, pp. 4–8, http://dx.doi.org/10.2514/6.2016-0997.

- [14] N.A. Hagen, M.W. Kudenov, Review of snapshot spectral imaging technologies, Opt. Eng., Bellingham 52 (9) (2013) 090901, http://dx.doi.org/10.1117/1.OE. 52 9 090901
- [15] B.K. Ford, M.R. Descour, R.M. Lynch, Large-image-format computed tomography imaging spectrometer for fluorescence microscopy, Opt. Express 9 (9) (2001) 444–453, http://dx.doi.org/10.1364/OE.9.000444, URL https://opg.optica.org/ oe/abstract.cfm?URI=oe-9-9-444.
- [16] W. Johnson, D. Wilson, W. Fink, M. Humayun, G. Bearman, Snapshot hyper-spectral imaging in ophthalmology, J. Biomed. Opt. 12 (2007) 014036, http://dx.doi.org/10.1117/1.2434950.
- [17] M.S. Peters, R.L. Eriksen, B. Jørgensen, High-resolution snapshot hyperspectral computed tomography imaging spectrometer: Real-world applications, in: M.P. Georges, G. Popescu, N. Verrier (Eds.), Unconventional Optical Imaging III, vol. 12136, International Society for Optics and Photonics, SPIE, 2022, p. 121360R, http://dx.doi.org/10.1117/12.2621128.
- [18] M. Ahlebaek, M. Peters, W.-C. Huang, M. Frandsen, R. Eriksen, B. Jørgensen, The hybrid approach – Convolutional neural networks and expectation maximization algorithm – for tomographic reconstruction of hyperspectral images, J. Spectr. Imaging 2 (2023) http://dx.doi.org/10.1255/jsi.2023.a1.
- [19] M.S. Peters, M.J.A. k, M.T. Frandsen, B. Jørgensen, C.H. Jessen, A.K. Carlsen, M.S. Andersen, W.-C. Huang, R.L. Eriksen, Investigating the applicability of a snapshot computed tomography imaging spectrometer for the prediction of brix and pH of grapes, Spectrochim. Acta Part A: Mol. Biomol. Spectrosc. 336 (2025) 126017, http://dx.doi.org/10.1016/j.saa.2025.126017, URL https://www.sciencedirect.com/science/article/pii/S1386142525003233.

- [20] L. Yuan, Q. Song, H. Liu, K. Heggarty, W. Cai, Super-resolution computed tomography imaging spectrometry, Photon. Res. 11 (2) (2023) 212–224, http://dx.doi.org/10.1364/PRJ.472072, URL https://opg.optica.org/prj/abstract.cfm? URI=prj-11-2-212.
- [21] H. Li, X.-F. Liu, X.-R. Yao, X.-Q. Wang, G.-J. Zhai, Snapshot compressed sensing computed-tomography imaging spectrometry, Opt. Laser Technol. 170 (2024) 110158, http://dx.doi.org/10.1016/j.optlastec.2023.110158, URL https://www. sciencedirect.com/science/article/pii/S0030399223010514.
- [22] W.-C. Huang, M.S. Peters, M.J. Ahlebæk, M.T. Frandsen, R.L. Eriksen, B. Jørgensen, The application of convolutional neural networks for tomographic reconstruction of hyperspectral images, Displays 74 (2022) 102218, http://dx.doi.org/10.1016/j.displa.2022.102218, URL https://www.sciencedirect.com/science/article/pii/S014193822200052X.
- [23] N. Hagen, E.L. Dereniak, D.T. Sass, Fourier methods of improving reconstruction speed for CTIS imaging spectrometers, in: S.S. Shen, P.E. Lewis (Eds.), in: Imaging Spectrometry XII, vol. 6661, International Society for Optics and Photonics, SPIE, 2007, 666103, http://dx.doi.org/10.1117/12.732669.
- [24] Q. Li, Y. Wang, X. Ma, W. Du, H. Wang, X. Zheng, D. Chen, A low-rank estimation method for CTIS image reconstruction, Meas. Sci. Technol. 29 (9) (2018) 095401, http://dx.doi.org/10.1088/1361-6501/aad1e6.
- [25] B. Birch, F. Zander, D.R. Buttsworth, L. Noller, A. Payne, Hayabusa2 capsule re-entry: Australian airborne observation emission spectroscopy calibration and preliminary analysis, in: AIAA SCITECH 2022 Forum, http://dx.doi.org/10.2514/ 6.2022-2151.